Magnetic QCA Majority Voter Feasibility Analysis

A 4-yr Climatology of Pressure Disturbances Using a Barometer Network in Central Illinois

S. GRIVET-TALOCIA* AND F. EINAUDI

Laboratory for Atmospheres, NASA/Goddard Space Flight Center, Greenbelt, Maryland

W. L. CLARK AND R. D. DENNETT+

NOAA/Aeronomy Laboratory, Boulder, Colorado

G. D. NASTROM

Department of Earth Sciences, St. Cloud State University, St. Cloud, Minnesota

T. E. VANZANDT

NOAA/Aeronomy Laboratory, Boulder, Colorado

(Manuscript received 6 January 1998, in final form 28 July 1998)

ABSTRACT

This paper presents a climatology of coherent disturbances detected during 1991–95 by a network of barometers with a diameter of about 50 km located in a very flat terrain centered on the Flatland Atmospheric Observatory in east-central Illinois. An automatic, wavelet-based adaptive filter is used to extract the waveforms of all disturbance events with amplitudes larger than a frequency-dependent threshold. The extracted events cover characteristic temporal scales from about 30 min to 6 h, that is, the range that includes mesoscale disturbances that affect the weather and the forecasts.

The analysis resulted in two classes of events. One class, called coherent events, or CEs, consists of disturbances that propagated coherently through the barograph network and for which the phase propagation velocity, dominant period, and horizontal wavelength could be estimated with good accuracy. The propagation directions of 97% of the CEs were between 0° and 180° (i.e., had an eastward component) and the speeds of 96% were between 10 and 50 m s^{-1} with a mode at 25–30 m s^{-1}. The other class, called incoherent events, or IEs, consists of disturbances that had significant amplitudes but that did not propagate coherently across the network, so that the propagation velocity could not be estimated. This class consists of localized disturbances and wave packets with short periods and/or wavelengths, or with pressure signatures that were too different at the network stations. The extracted events are attributed to gravity waves, wave packets, gravity currents, pressure jumps, solitary waves, bores, etc.

The rate of occurrence of events had a strong seasonal dependence, with a maximum in fall and winter and a minimum in summer. The CEs occurred about 20%–21% of the total time in fall and winter and 12% in summer, while all events occurred 34% in both fall and winter and 23% in summer. The seasonal dependence of events confirms the strong relation of these disturbances to the baroclinicity of the atmosphere.

Concurrent vertical velocity fluctuations observed by the 50-MHz radar at the Flatland Atmospheric Observatory showed that many of the large-amplitude events extended up to at least 7 km, the highest altitude reliably observed by the radar.

1. Introduction

This paper presents a 4-yr climatology of wavelike disturbances in the pressure field that propagate across a network of barometers near Champaign–Urbana, Illinois. These disturbances may include (i) events with periods of the order of minutes and wavelengths of the order of a few kilometers, generated by wind shear below the jet maxima (Herron and Tolstoy 1969; Mastrantonio et a1. 1976; Bedard et al. 1986; Hooke and Hardy 1975); (ii) disturbances generated by shear or other mechanisms lower in the atmosphere, including within the boundary layer, which generate and/or interact with turbulence and convection in the boundary layer and couple the boundary layer with the atmosphere above (Einaudi and Finnigan 1981; Clark and Thomas 1986; Hauf and Clark 1989); (iii) solitary waves and

* Additional affiliation: Science Systems and Applications, Inc., Lanham, Maryland.

+ Additional affiliation: Cooperative Institute for Research in Environmental Studies, Boulder, Colorado.

Corresponding author address: Dr. Stefano Grivet-Talocia, Politecnico di Torino, C. Duca degli Abruzzi, 24, I-10129 Torino, Italy. E-mail: grivet@polito.it

bores (Smith 1988; Fulton et al. 1990; Christie 1989, 1992); (iv) mesoscale disturbances with periods of the order of hours and horizontal wavelengths of the order of hundreds of kilometers, which interact with and sometimes trigger convection (Bosart and Cussen 1973; Uccellini 1975; Balachandran 1980; Stobie et al. 1983; Uccellini and Koch 1987; Ferretti et al. 1988; Schneider 1990; Ralph et al. 1993; and others). All these disturbances will be denoted generically as gravity waves throughout the paper.

Gravity waves play an important role in atmospheric dynamics because they can transport energy and momentum over large distances both horizontally and vertically. This role has been parameterized in general circulation models (GCMs). Topographically induced gravity waves have been shown to influence the strength and position of the polar jet and the temperature field in the troposphere (McFarlane 1987) and in the stratosphere and the mesosphere (Bacmeister 1993). Fritts and Lu (1993) and Hines (1997a,b) have developed a parameterization scheme that assumes the existence in the lower troposphere of a spectrum of upward propagating gravity waves that describes reasonably well the latitudinal and seasonal variations in the zonal winds and latitudinal temperature gradients of the upper mesosphere. See also Mengel et al. (1995), Mayr et al. (1997a,b), and Warner and McIntyre (1996).

At the mesoscale, gravity waves play the same fundamental role that Rossby waves play at the synoptic scale. Since they cover the entire range of spatial scales from frontal systems down to convective cells, they are the link between synoptic- and smaller-scale motions. They can have amplitudes of several hectopascals and they can induce rapid and sometimes major changes in otherwise well-forecast, synoptic-scale weather conditions. For example, Schneider (1990) described a disturbance that 1) produced a surface pressure deeper than a rapidly developing cyclone, 2) involved pressure tendencies (11 hPa in 15 min) that far exceed the criterion used for explosive cyclogenesis, and 3) enhanced precipitation rates in relatively narrow bands. Such disturbances create a substantial challenge for the research and forecast community. Thus, part of the difficulties that forecasters face is that these large mesoscale disturbances are not explicitly predicted by the current operational models. Even the climatology of these events is at present poorly known. Clearly, local weather forecasts could be helped considerably by a comprehensive documentation of these mesoscale waves, their characteristics, their areas of development, their source mechanisms, and the synoptic settings within which they develop and with which they interact. Mesoscale models with higher resolution have improved our understanding of the role of gravity waves at these scales (Schmidt and Cotton 1990; Pokrandt et al. 1996; Powers 1997). Indeed, the improved resolution of the current generation of operational models supports identification of gravity waves in the model output, although there are few observational studies with which to compare such results (Barnes et al. 1996).

Only sparse information exists on the climatology of gravity waves, that is, the statistics of their speed and direction of propagation, frequency of occurrence, amplitudes, temporal and spatial characteristic scales, and vertical structure. Some climatologies of wavelike disturbances in the troposphere, stratosphere, and mesosphere have been developed with data from rockets (Hirota 1984; Hirota and Niki 1985), balloons (Kitamura and Hirota 1989; Allen and Vincent 1995; Nastrom et al. 1997), lidars (Wilson et al. 1991), and radars (Sato 1994; Murayama et al. 1994). Other studies have been based on surface pressure data (Einaudi et al. 1989; Hauf et al. 1996; Koppel et al. 1999, and references therein). Since the pressure at the ground varies in response to changes in the mass of the overlying atmosphere and to vertical accelerations, it is thus a good indicator of gravity waves. In fact, pressure records are less noisy than temperature, wind, or humidity records because the inherent integration over height acts as a filter. Even so, pressure-based climatological studies of these disturbances are rare because the analysis is complex. Some of the difficulties are outlined in Grivet-Talocia and Einaudi (1998, henceforth denoted GE98).

In this work we present a climatology of mesoscale gravity waves based on pressure time series from a network, which had a diameter of about 50 km, of six or seven digital barometers. With this network we were able to investigate disturbances with temporal scales from tens of minutes to a few hours and spatial scales from a few tens to several hundred kilometers.

A network of at least three barometers may allow determination of the horizontal velocity of propagation of a wave event, which, in conjunction with the frequency content from analysis of the time series of the signal, provides information on the horizontal scales of the event. Since each of the atmospheric processes that generate wavelike disturbances has its own footprint in the surface pressure, different types of disturbances may require different kinds of analyses. When the pressure record is nearly monochromatic, as in the event analyzed by Einaudi and Finnigan (1981), the waveform can be efficiently obtained by a bandpass filter, which can be optimally designed using a standard FFT analysis. This technique assumes the decomposition of the event into a superposition of a few sinusoids, thus allowing a sharp frequency resolution. More often, the signal is complex and localized in time, such as short wave packets and solitary waves. Mesoscale phenomena such as thunderstorms go through a sequence of stages that leave various signatures in the pressure field and make the analysis of the records quite difficult. These cases are characterized by broad frequency bands due to their time localization. A set of bandpass filters could be used to extract all the energy of the disturbance from the time series. This process would lead to a set of smoothed waveforms in each frequency band, each one having

little resemblance to the original disturbance. When processing each band independently, spurious correlations among the signals at the network stations would be introduced, producing erroneous calculated propagation velocities. In other words, a good determination of the event waveform is essential for obtaining accurate estimates for its speed and direction of propagation.

The wavelet transform method outlined in section 3 and described in more detail in GE98 satisfies this need, because it allows an accurate and efficient detection and extraction of the events in general and of the mesoscale events in particular. Wavelet transforms have recently been used in several studies of atmospheric dynamics (e.g., see the references in Lau and Weng 1995 and GE98). Hauf et al. (1996) applied wavelet analysis to barograph data, but their network was much smaller than ours and they analyzed only a small amount of data. Also, the various studies have used several different mother wavelets, appropriate to their particular database.

As with the standard FFT, the wavelet transform allows the decomposition of a signal into a set of basis functions, but these are localized in both time and frequency. This allows the time and frequency components of a disturbance to be considered simultaneously and minimizes the introduction of spurious correlations. GE98 also developed an algorithm that separates the events into two main classes, here called coherent events or incoherent events (henceforth abbreviated CEs or IEs, respectively), according to their degree of coherence across the network of barometers. The horizontal velocity can be estimated only for the coherent events. A precise definition of the criteria discriminating the two classes will be found in section 3.

We have estimated the depth of some of the events using data from the 50-MHz wind-profiling radar located at the Flatland Atmospheric Observatory (FAO). We find that most of the large-amplitude events extended up to at least 7.0 km, the highest altitude consistently observed by the radar.

We also attempt to relate our statistical results to meteorological features. The limitations and qualitative nature of such comparisons are described. They stem from the complex nature of weather and the difficulties in analyzing all the various weather data in an automatic process.

The barometer network and the data are described in section 2, while the wavelet method is outlined in section 3. The statistical results are presented and discussed in section 4 and are compared with meteorological events in section 5 and 6.

2. Experimental setup

This section describes the experimental setup and the dataset that will be processed in the following. Figure 1 shows the network of eight digital barometer sites that were used in this study, although only six or seven of them were operational at the same time. The central station, FLA, is located at FAO at 40.05°N, 88.38°W, near Champaign–Urbana, Illinois. This network differs from previous barometer networks in three respects. First, it is much larger, spanning about 50 km. Second, the terrain in and around the network is extremely flat, with the altitude difference between the highest and lowest stations, WIL and TUS, being only 25 m. Third, the barometers are digital rather than analog, which permits study of long-period fluctuations. The barometers are located in offices to shield them from wind and rapid temperature fluctuations. Each station instantaneously samples the pressure every 10 s and archives a block average of 12 samples every 120 s, which is then the effective sampling interval. The resulting precision is about 10^{-2} hPa. Once a day the 120-s means are transferred by telephone to a computer database at the National Oceanic and Atmospheric Administration (NOAA) Aeronomy Laboratory in Boulder, Colorado.

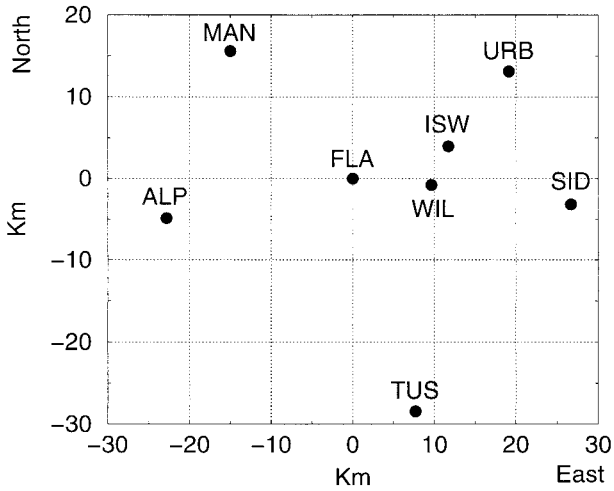

FIG. 1. Geometry of the Flatland barometer network. The coordinate system is centered on the reference station located at Flatland (FLA). The other stations are Allerton Park (ALP), Illinois State Water Survey (ISW), Mansfield (MAN), Sidney (SID), Tuscola (TUS), Urbana (URB), and Willard (WIL).

At the beginning of 1991 the network consisted of six stations (lacking ISW and WIL). On day 336 of 1991 station ISW was installed, on day 272 of 1992 station ALP was shut down, and on day 18 of 1993 that instrument was relocated to WIL. Thenceforth the network was not changed. Therefore, the number of stations that recorded data simultaneously was usually seven but sometimes only six.

Data were analyzed from 15 quarters spread over five calendar years, from the beginning of 1991 to the end of 1995. Several problems, including interruptions of the telephone links and malfunctioning of the data recording system, reduced the size of the usable dataset. The years 1991 and 1992 are complete, while only parts of 1993, 1994, and 1995 are available as shown in Table 1. The quarters are defined by the day intervals in col-

TABLE 1. List of data used in this study. The number of analyzable days is given for each quarter.

Quarter	Days	Months	1991	1992	1993	1994	1995	Total
1	1.0–91.0	JFM	90	90	89	31	—	300
2	91.0–182.0	AMJ	91	91	91	82	—	355
3	182.0–274.0	JAS	92	89	92	—	92	365
4	274.0–366.0	OND	89	88	—	—	92	269

umn two, while the months in column three are only nominal.

Since the configuration and separation of the stations limits the spatial and temporal scales of disturbances that can be correctly identified and processed, as will be shown later, the present study concentrates on mesoscale disturbances. Synoptic and tidal fluctuations are eliminated by preprocessing the raw pressure time series with a highpass filter with a cutoff at six hours. By repeating the entire analysis with data highpass filtered with a cutoff at eight hours we found that the results are insensitive to the cutoff period. The highpass-filtered pressure time series will be denoted henceforth by $f_i(t)$, where the subscript i denotes the stations, with $i = 1$ for FLA.

3. Data processing

This section describes the data processing technique used in this paper, which allows the iterative detection, extraction, classification, and analysis of pressure events from the network of barometers. The technique is based on a selective reconstruction of the waveform of an event that is coherent through the network. This is achieved through the partial inversion of the wavelet transform of the pressure data at the different stations combined with cross-correlation techniques. In a second stage, the arrival times of the wave event at the network stations are used to determine its speed and direction of propagation.

The wavelet algorithm used in this paper is described in detail in GE98, so only a summary of the main steps and their theoretical justification will be given here. Many excellent introductory books on the wavelet transform have already been published (Daubechies 1992; Chui 1992; Meyer 1992). We will give here only the few definitions that are strictly necessary to understand the data processing technique. Note that in the present paper the notation for the wavelet transform has been simplified with respect to GE98.

Let us consider a function $\psi(t)$ that is localized both in time and frequency. In other words, both $\psi(t)$ and its Fourier spectrum $\hat{\psi}(\omega)$, where ω is the frequency, have significant magnitudes only on a finite interval of the time and frequency axis. The function $\psi(t)$ is denoted mother wavelet. A set of dilated and translated versions of ψ is derived through

$$\psi_{b,a}(t) = \frac{1}{|a|}\psi\left(\frac{t-b}{a}\right). \quad (1)$$

The parameter b shifts the wavelet in time, while a, usually called the scale, modifies its dominant period T (or equivalently its dominant frequency, which is inversely proportional to a). Since the functions $\psi_{b,a}(t)$ have a constant shape, they preserve the time–frequency localization of the mother wavelet. The time localization is tuned by the parameter b, and the frequency localization by the parameter a. When the signal $f(t)$ is real and when the mother wavelet is *progressive*, that is, its Fourier spectrum is identically zero for negative frequencies, see Grossmann et al. (1989), we can restrict the analysis to positive values of a. The resulting expressions for the wavelet transform and its inverse are (Daubechies 1992)

$$W(b, a) = \langle f, \psi_{b,a}\rangle \equiv \frac{1}{|a|}\int_{-\infty}^{+\infty} f(t)\psi^*\left(\frac{t-b}{a}\right) dt, \quad (2)$$

$$f(t) = \frac{2}{C_\psi}\int_0^{+\infty}\frac{da}{a}\int_{-\infty}^{+\infty} db\ \Re\{W(b, a)\psi_{b,a}(t)\}, \quad (3)$$

where $\Re$ denotes the real part. Note that we use here the L^1 normalization instead of the more standard L^2 normalization, because it allows a simple link (independent of the parameter a) between the amplitude of the disturbances and the magnitude of the wavelet transform (see GE98). The only necessary condition for these equations to be true is the so-called admissibility condition (Daubechies 1992),

$$C_\psi = \int_{-\infty}^{+\infty}\frac{|\hat{\psi}(\omega)|^2}{|\omega|}\, d\omega < \infty, \quad (4)$$

which essentially requires that the mother wavelet be a bandpass filter. The mother wavelet used in this paper is the analytical signal associated to the fourth derivative of a Gaussian (see GE98). This progressive wavelet has been chosen due to its good time–frequency localization properties.

Equation (3) means that the signal $f(t)$ is exactly decomposed into a superposition of basis functions that are localized in both time and frequency. Therefore, the magnitude of the wavelet transform $|W(b, a)|$ indicates the presence in the signal $f(t)$ of a particular period T (proportional to a) at a particular time b. This localization in time is the advantage of the wavelet transform with respect to the Fourier transform. We will show that the wavelet decomposition is indeed a suitable tool for the study of disturbances such as solitary waves or short wave packets.

The inversion of the wavelet transform in Eq. (3) is achieved by integrating over the whole semiplane $\Sigma = \{(b, a)\,|\,a > 0\}$. If, however, the characteristics of a particular feature or event are of interest, then $W(b, a)$ can be considered over only a smaller domain $\Omega \subset \Sigma$. This allows study of the time–frequency components of

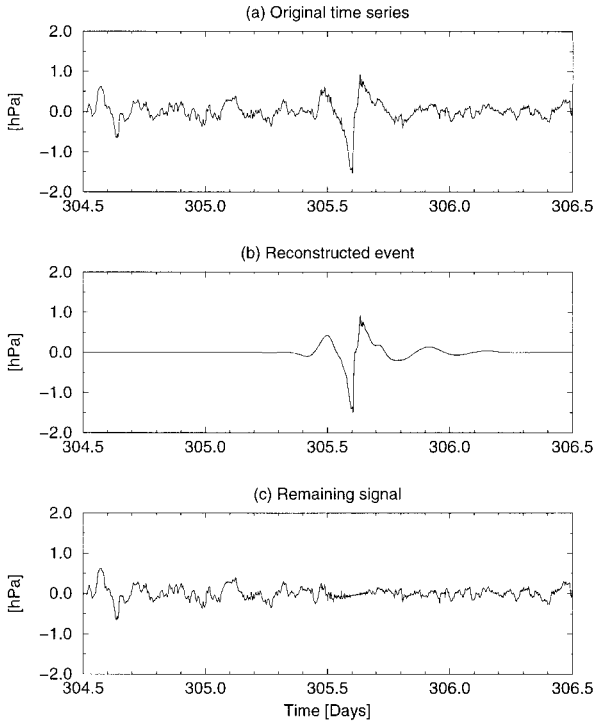

FIG. 2. Extraction of a single event at FLA in November 1991: (a) the original highpass-filtered pressure series $f_1(t)$, (b) the extracted event $p_1(t)$, and (c) the residual waveform $f_1(t) - p_1(t)$.

that particular event separately from other events and geophysical noise. The waveform $p(t)$ of the event can then be extracted using Eq. (3) by integrating a and b over only Ω. The problem is then to develop an automatic procedure to determine Ω from $f(t)$, so that the extracted signal includes only the event under investigation and is identically zero elsewhere. As a result, the process of extracting $p(t)$ can be interpreted as a nonlinear adaptive filter, expressed by

$$p(t) = \frac{2}{C_\psi} \int\int_\Omega \frac{da\ db}{a} \Re\{\langle f, \psi_{b,a}\rangle \psi_{b,a}\}. \qquad (5)$$

The method of determining Ω is illustrated by application to the two-day pressure time series $f_1(t)$ observed at FLA shown in Fig. 2a. The corresponding contours of $|W(b, a)|$ are shown in Fig. 3a as a function of time and frequency or period. The large amplitudes of the contours centered at days 304.6 and 305.6 suggest that these may represent events. The simultaneous contours of $|W(b, a)|$ at URB shown in Fig. 3b are well correlated with FLA during the events, but not outside of the events. The poorly correlated values outside of the events are due to some kind of local geophysical noise.

In order to identify an event objectively we require that the maximum of $|W(b, a)|$ during the event must exceed a threshold function $A(a)$, which is scale dependent (i.e., period dependent), because previous studies (Gossard 1960; Bull et al. 1981; Canavero and Einaudi 1987) showed that the amplitude of the background pressure fluctuations is an increasing function of the

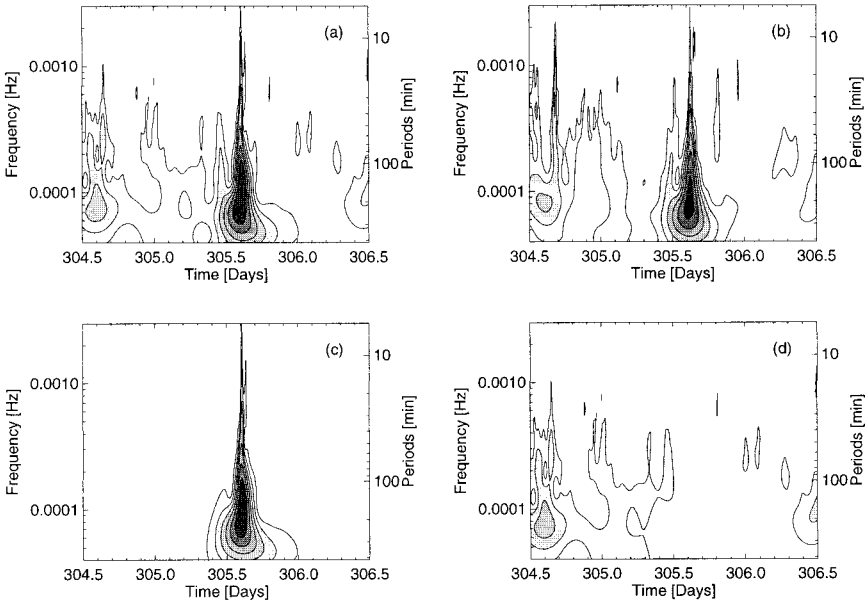

FIG. 3. Wavelet transforms shown as contour plots: (a) the highpass-filtered signal $f_1(t)$ at FLA shown in Fig. 2a, (b) $f_i(t)$ at URB, (c) the extracted event $p_1(t)$ shown in Fig. 2b, and (d) the remaining signal $f_1(t) - p_1(t)$ shown in Fig. 2c. The intensity of the grayscale is proportional to the wavelet transform magnitude $|W(b, a)|$.

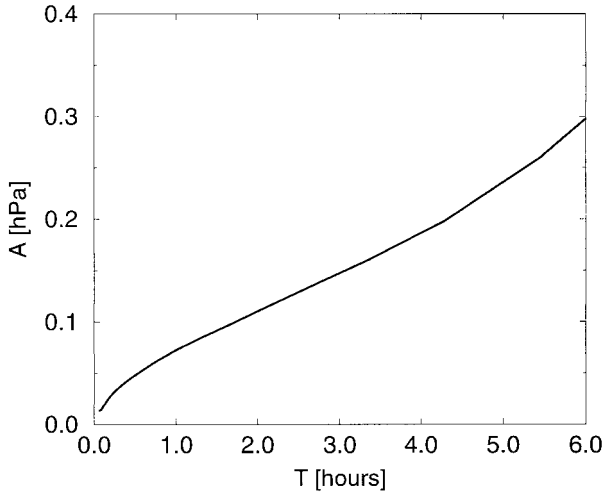

FIG. 4. The scale-dependent threshold function $A(a)$ plotted vs period T, which is proportional to the scale parameter a.

period. Plotted in Fig. 4, $A(a)$ is defined as the time average of $|W(b, a)|$ evaluated over the entire data stream; that is,

$$A(a) = K\langle |W(b, a)| \rangle_b, \tag{6}$$

where K is an appropriate normalization constant (see GE98). This threshold can be regarded as the average amplitude of pressure fluctuations at a given scale a.

Thus, an event is identified by a maximum of $|W(b, a)|$ at (b_c, a_c) with a magnitude larger than $A(a_c)$. The domain Ω of the event is then determined by extending in all directions from (b_c, a_c) until the first directional minimum of $W(b, a)$ is encountered. This method includes most of the energy of the event while minimizing inclusion of fluctuations due to other events or geophysical noise.

The wavelet inversion through Eq. (5) leads to the extracted waveform of the event $p_1(t)$, shown in Fig. 2b. Figure 3c shows its time–frequency components. Figures 2c and 3d show the waveform and the time–frequency components of the residual $f_1(t) - p_1(t)$.

The domain of an event at FLA, denoted Ω_1, is determined first. Then for each other station i the corresponding domain Ω_i is determined under the hypothesis that the event is a coherent disturbance propagating with small distortions through the barograph network. A first estimate of Ω_i at station i is obtained by time shifting Ω_1 by the propagation delay time between the two stations, Δb_{opt}, that maximizes the cross-correlation function

$$G_{1i}(\Delta b) = \iint_{\Omega_1} \frac{da\, db}{a} \Re\{W_1(b, a)\} \Re\{W_i(b + \Delta b, a)\}, \tag{7}$$

where $W_i(b, a)$ indicates the wavelet transform of the pressure signal $f_i(t)$ at station i. This function selects only those time–frequency components included in Ω_1.

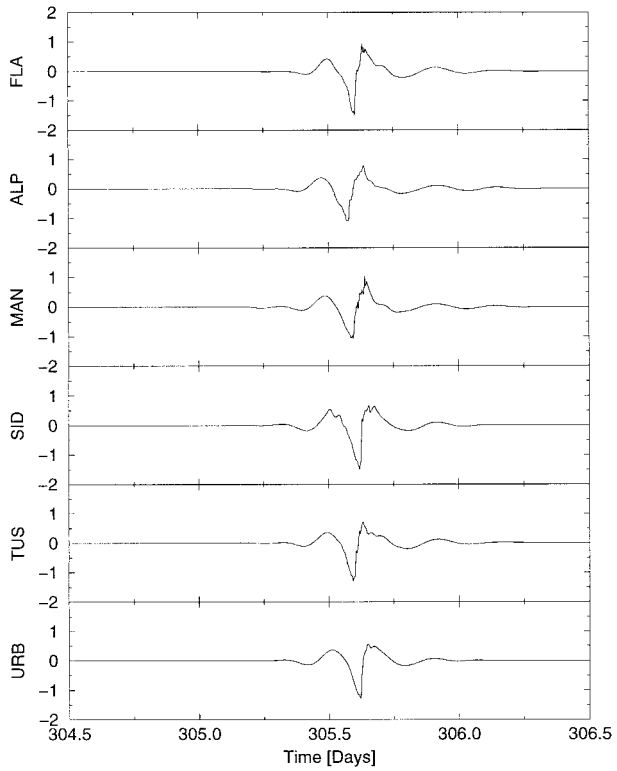

FIG. 5. Extracted waveforms $p_i(t)$ at the available stations for the event plotted in Fig. 2. The vertical axis is pressure in units of hPa.

Then the coordinates of the maximum of $|W_i(b, a)|$ within the domain Ω_1 translated by Δb_{opt} are found and Ω_i is determined by the steps already described for the reference station. This selective cross-correlation procedure ensures that the same event is identified at each station, but it permits inclusion of local distortions in the corresponding extracted waveform $p_i(t)$. This is evident in Fig. 5, where the waveforms $p_i(t)$ of the event in Fig. 2 are plotted for all six stations that were operating at that time. Although the main shape of the disturbance is the same at each station, the details are different.

A refined estimate for the delay times

$$\Delta t_i = t_i - t_1, \qquad i = 2, \ldots, N_s \tag{8}$$

between each station i and FLA is now obtained as the value of τ that maximizes the cross-correlation function

$$C_{1i}(\tau) = \frac{1}{\|p_1\| \|p_i\|} \int p_1(t) p_i(t + \tau)\, dt. \tag{9}$$

There are two considerable advantages in calculating the Δt_i from the extracted $p_i(t)$ rather than attempting to do so from the highpass-filtered $f_i(t)$. First, this minimizes the influence of fluctuations that do not belong to the event under consideration. Second, the integration interval is automatically determined by the finite duration of the $p_i(t)$. If the $f_i(t)$ were used instead of the $p_i(t)$, then the integration domain would be undefined

because the duration of the event is not known a priori. A measure for the coherency through the network is given by the mean of the cross-correlation coefficients, $\overline{C} = \langle C_{1i}(\Delta t_i)\rangle$.

The velocity, that is, the speed and direction, of the event can now be determined from the set of Δt_i. We hypothesize that the disturbance is a plane wave at the scale of the observing array, so that at station i,

$$p_i(t) = p_1(t - \mathbf{r}_{1i} \cdot \mathbf{s}), \tag{10}$$

where $\mathbf{r}_{1i}$ is the distance vector between station 1 (FLA) and station i, and $\mathbf{s}$ denotes the slowness vector (Einaudi 1995). The slowness vector points in the direction of wave propagation, and its magnitude is the reciprocal of the horizontal phase speed. The speed and direction are estimated by fitting this model to the set of delay times Δt_i with a standard least squares criterion. The fitting error is expressed by δt_{rms}, defined as the mean rms deviation between the measured and the model propagation delays, normalized by the sampling time.

As a result of this procedure, events are separated into two different classes.

- Coherent events (CEs; called class 1 in GE98): A CE is an event with a large mean cross-correlation coefficient ($\overline{C} > 0.75$) and a small fitting error ($\delta t_{\text{rms}} < 3$). Thus, a CE is a well-identified event that propagates coherently across the network and for which the propagation velocity (speed and direction), and wavelength, as well as the duration, amplitude and period band, can be determined.
- Incoherent events (IEs; called class 2 in GE98): An IE is an event with small $\overline{C}$ and/or large δt_{rms}, that is, not satisfying the criteria described above. Such an event can be a localized disturbance that does not propagate through the entire network, a wave packet with a wavelength that is small with respect to the dimension of the network, or an event with excessive superimposed geophysical noise. For an IE, only the duration, amplitude, and period band can be determined.

A few comments are in order about the threshold values mentioned above. On one hand, the cross-correlation coefficients are quite large when compared to other studies (see, e.g., Einaudi et al. 1989). Therefore, it might seem that our criterion is too restrictive, in the sense that waves with significant cross-correlations are rejected. This is not the case, because the wavelet-based event extraction tool is highly optimized, and so it permits computation of the cross-correlation coefficients with high reliability and with almost no influence of the data processing technique on the results. This results in larger cross-correlation coefficients with respect to those obtained through a nonoptimized bandpass filter. On the other hand, a plane wave fitting error of δt_{rms} might seem too large since it translates into an average positional error of about 9 km for a wave with 25 m s^{-1} speed, corresponding to about 35% of the average distance between the network stations. We chose this value because we also want to include in our results waves without perfectly straight phase fronts. The estimated phase speed and propagation direction will be, in effect, an average computed through the network. Of course, only those waves with high coherency (i.e., large cross-correlations) will not be rejected. Finally, it should be noted that the amplitude is not a criterion for the classification of CEs and IEs. The reader is referred to GE98 for a more detailed description of the statistical tests leading to the classification.

The time-averaged wavelet spectrum $\mathcal{E}_i(a)$ at each station i is defined as

$$\mathcal{E}_i(a) = \int |W_i(b, a)|^2 \, db. \tag{11}$$

A mean wavelet spectrum for each event is then obtained by averaging $\mathcal{E}_i(a)$ over all stations to form

$$\overline{\mathcal{E}}(a) = \langle \mathcal{E}_i(a)\rangle_i. \tag{12}$$

The dominant period T_m of each event corresponds to the value of a at the maximum of $\overline{\mathcal{E}}(a)$. For CE the horizontal wavelength λ is also estimated as $\lambda = vT_m$, where v is the phase speed. The value of T_m is of course only indicative, since a nonmonochromatic disturbance is characterized by a band of periods centered around T_m. This period band is here defined as the interval including the central 50% of the total energy in $\overline{\mathcal{E}}(a)$. Similarly, the duration of an event is here defined as $\Delta T = t_e - t_s$, where t_s and t_e are the times at the 1% and 99% levels of the cumulative instantaneous energy; thus, ΔT includes 98% of the total event energy. The amplitude of each event is simply defined as the average of the maximum peak-to-peak fluctuations at the different stations.

The procedure described above permits extraction and study of a single event. The event with the largest amplitude at FLA was detected first, its reconstructed waveform $p(t)$ was subtracted from the highpass-filtered pressure trace $f(t)$ at all stations, the next largest event was detected, and the extraction procedure was iterated until all events above an amplitude threshold (derived in GE98) were processed. It is shown in GE98 that the application of a number of statistical consistency tests to the iterated extraction procedure ensures that wrong identifications are avoided. Thus, all significant events were extracted and global statistics and climatological results were obtained.

For example, when the analysis procedure described above was first applied to the $f_i(t)$ from day 304.5 to 306.5 1991 ($f_1(t)$ for FLA is shown in Fig. 2a), a coherent event was found centered at 305.6. The reconstructed waveforms are shown for all six stations in Fig. 5. However, when the procedure was applied to the residuals (see Fig. 2c) no event was found at 304.6 because the results did not satisfy the criteria on $\overline{C}$ and δt_{rms}.

The described method is very powerful for the study of disturbances that are localized in time. However, there are some disadvantages for the analysis of some other kinds of disturbances, such as long-lasting, nearly monochromatic, short-period wave trains. Sharp time localization is not critical for such events, but a precise definition of the period is needed. This could be estimated from the wavelet period spectrum $\overline{\mathcal{E}}(a)$, but with low precision. In addition, the wavelet reconstruction includes all the significant time–frequency components that are in the extracted waveforms. If longer-period amplitude modulations are present with amplitudes that are comparable with or larger than the amplitude of the shorter-period event, then the inferred shorter-period phase velocity may be incorrect. Such problems could be avoided by using a sharp bandpass filter centered on the frequency determined by the FFT, with sacrifice of temporal resolution. In any case, the timescales that are investigated in this paper are so long that a wave packet with many cycles would last for several days; such a disturbance was never detected in our pressure records. When a smaller-size network is analyzed or when this data processing technique is applied to other datasets of different nature, such as seismic signals or ocean waves, more care should be taken for the mentioned cases.

4. Results

a. Statistics of wavelet pressure events

The iterative algorithm summarized in section 3 has been applied to the data listed in Table 1. Of the 1301 days with usable data, a total number of 1690 events were identified, of which 626 were CEs and 1064 were IEs. There were some intervals lasting several days during which no wave events were detected. GE98 illustrated the application of this process by displaying each of the CEs detected during a 21-day period in the winter of 1991. In this section the statistical properties of all of the CEs and IEs will be discussed.

Most of the detected events fall into one of the five types itemized below: (I) positive pressure spike, (II) negative pressure spike, (III) negative pressure jump, (IV) positive pressure jump, and (V) wave packet. About 40% of the CEs are of the types I through IV, that is, display features typical of solitary waves. All types are illustrated in the different rows of Fig. 6 by examples from FLA. The raw unfiltered pressure traces are shown in the left column, and the extracted waveforms $p(t)$ are shown in the right column (with an enlarged amplitude scale). It should be noted that in the extracted waveforms, which have zero means, the overshoots before and after the main feature may be caused by the preprocessing highpass filter described in section 2. This does not affect the climatological results.

1) SPEED AND DIRECTION OF PROPAGATION

The horizontal directions of propagation in degrees measured clockwise from north (e.g., a direction of 90° denotes propagation from west to east) and speeds in meters per second for the CEs are shown in Figs. 7 and 8, respectively. They are plotted sequentially in each of the quarters defined in Table 1. Each dot denotes the mean direction of propagation or the mean speed. The error bar was determined by fitting the equivalent plane wave model to each subset of three stations defining nonoverlapping regions and taking the maximum and minimum values. The bar, therefore, can be interpreted as the spatial variability of determined directions and speeds within the area encompassed by the network of stations. The histograms of direction and speed are plotted in Figs. 9 and 10, respectively. The left panels show the total number of detected events in each direction or speed bin, and the right panels show their frequency of occurrence, defined as the total duration of events in a given bin divided by the total analyzed time, expressed as a percentage. Ninety-seven percent of the directions were between 0° and 180° and 68% were between 45° and 135°. The speed distribution has a well-defined peak between 25 and 30 m s^{-1} and 96% of the speeds were between 10 and 50 m s^{-1}. Small speeds with long wavelengths and large speeds with short wavelengths cannot be detected by the network because of the 2-min time resolution of the pressure measurements and the 6-h highpass filter cutoff. However, the decreases on either side of the maxima in Fig. 10 are in ranges where the instrumental attenuation is weak; it appears that attenuation is significant only in the tails of the histogram where there were actually very few events.

2) PERIOD AND WAVELENGTH

Since the procedure described in section 3 for evaluating the dominant period T_m and the period band of each event does not require the knowledge of its speed and direction, these can be evaluated for IEs as well as for CEs. Figure 11 shows period histograms of (a) number of events and (b) their total duration divided by the total observation time, expressed as a percentage. The histograms were constructed as follows. The calculations involving the wavelet transform must be performed on a discrete grid of points in the timescale (b, a) plane, so we selected 20 logarithmically spaced scales (i.e., periods). Each bin in the histograms is bounded by two of those discrete periods. Since the period band of each event, defined in section 3, always extends into more than one point on the period axis, each event contributed to more than one bin in the histograms of Fig. 11. The thin lines represent all events, the thick lines represent CEs, and the difference represents IEs. The number of CEs with short periods is attenuated because, as mentioned in the previous sections, the possibility of determining the velocities of events decreases as their spatial scales become increasingly smaller than the size of the network. From Fig. 11a the lowest bin with any significant number of CEs is centered on 17.5 min. The histograms also show a

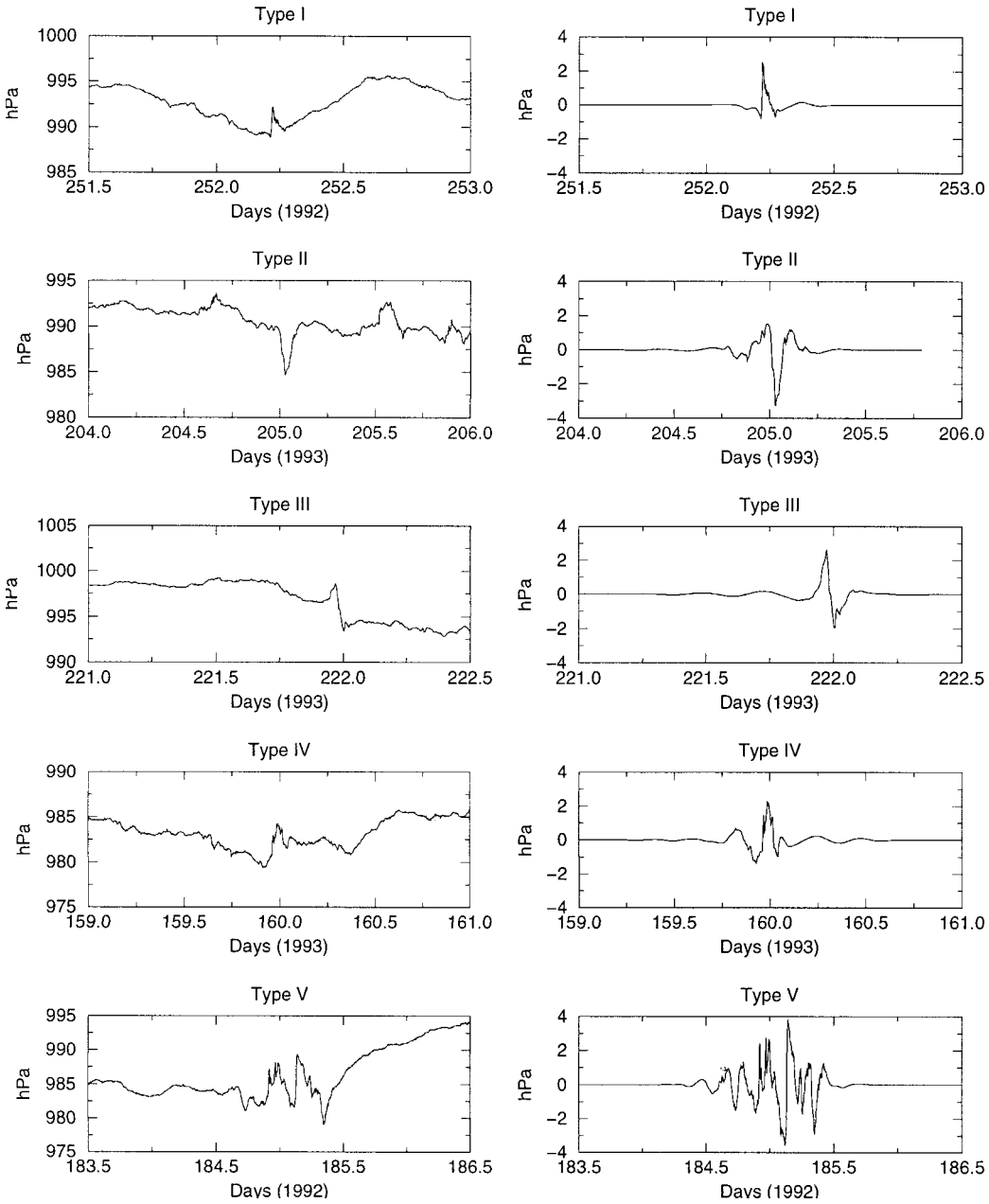

FIG. 6. Each row shows one of the event types. The raw, unfiltered pressure traces at FLA are shown in the left column, and the extracted waveforms $p(t)$ are shown in the right column.

sharp decay for periods longer than about 4 h due to the preprocessing highpass filter described in section 2, which removes periods longer than 6 h. In the period range between these two limits the number of CEs increases with increasing dominant period. The histogram in Fig. 11b has the same qualitative behavior but, of course, weighted toward longer periods.

The corresponding histograms of horizontal wavelength $\lambda = vT_m$ for CEs are shown in Fig. 12. Consistent with the foregoing remarks about filtering, very few events with horizontal wavelengths shorter than 40 km or longer than 600 km were detected; 96% of the wavelengths lay between these values.

3) AMPLITUDE

The amplitude is another important parameter associated with each event. At each station the amplitude is taken to be the difference between the maximum and minimum in the extracted waveform $p(t)$, illustrated in Fig. 5 and in the right-hand panels of Fig. 6. The mean amplitude is formed by averaging over all of the sta-

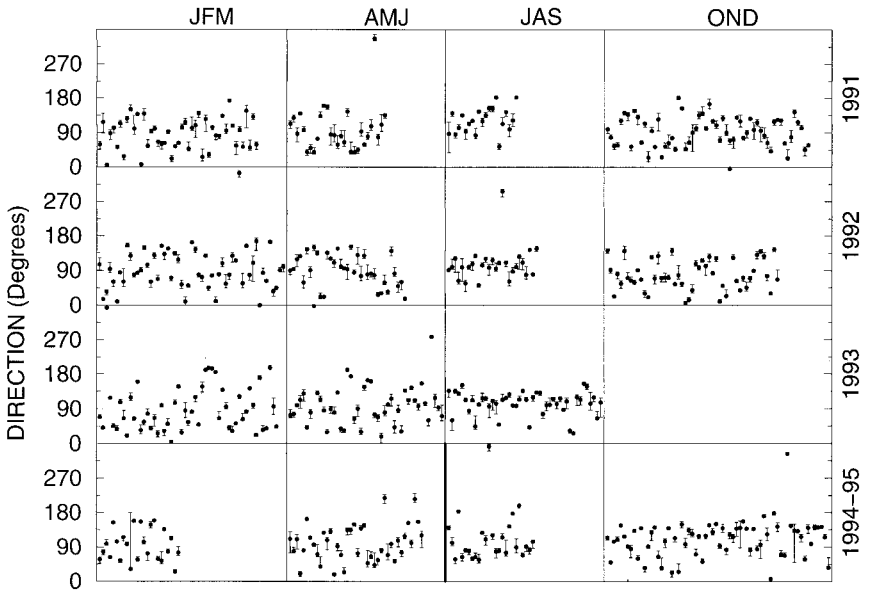

FIG. 7. Estimates of directions of propagation of coherent events (CEs) in order of extraction in each quarter defined in Table 1. The directions are given in degrees clockwise from north (see text), with the error bars indicating the variability across the network. In the last row the heavy vertical line separates the first two quarters of 1994 from the two last quarters of 1995.

tions. The mean amplitudes of the CEs and IEs are plotted in Figs. 13a and 13b, respectively, as scatterplots versus their dominant periods T_m. It is clear that the amplitude is a strong function of T_m. On the other hand, no significant correlation was detected between amplitude and speed or amplitude and wavelength (not shown here).

4) FREQUENCY OF OCCURRENCE AND SEASONAL VARIATION

Figures 14a and 14b show the percentage frequency of occurrence (total duration of events divided by total analyzed time) for CEs and for all events, respectively. The frequency of occurrence was determined in each quarter separately and then averaged over the different

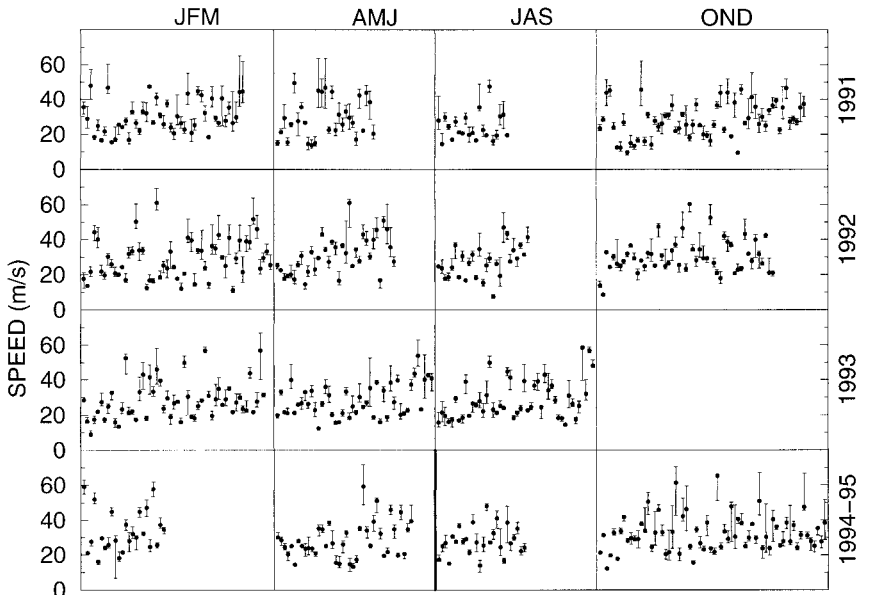

FIG. 8. Same as in Fig. 7 but for speed in m s^{-1}.

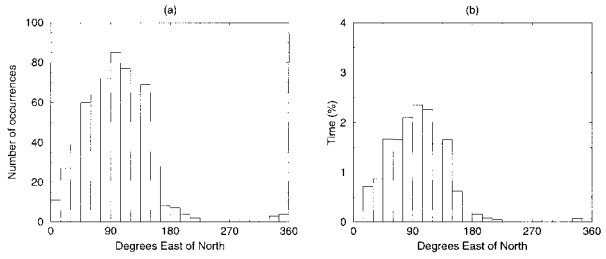

FIG. 9. Histograms of the direction of propagation (see text) of CEs measured clockwise from north. The vertical axis in (a) indicates the number of events and in (b) their frequency of occurrence expressed as a percentage of the total analyzed time.

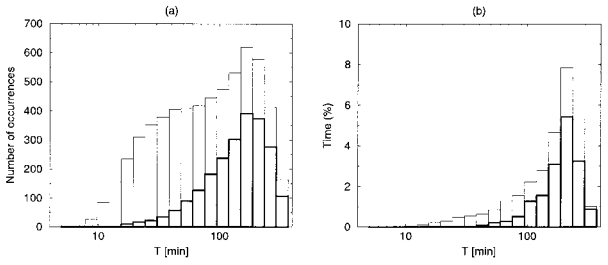

FIG. 11. (a) The number of events with period bands contributing to each bin is plotted for CEs (thick line) and all events (thin line, starting from 0). The difference between thin and thick line histograms corresponds to IEs. (b) As in (a) but the vertical axis indicates the frequency of occurrence as a percentage of the total analyzed time.

years. The standard deviation due to variations over the years is indicated by the error bars in the figure. There was a strong seasonal dependence, with a maximum in fall and winter and a minimum in summer. CEs occurred about 20%–21% of the time in fall and winter and 12% in summer, while all events occurred 34% in both fall and winter and 23% in summer.

b. Vertical structure

The vertical structure of the extracted events can be studied with the use of wind profiles obtained with the 50-MHz Doppler radar located at FAO. The radar observed profiles of radial wind in five directions, vertical and at 14.5° zenith angle in the N, E, S, and W azimuths, with a range resolution of 750 m in 16 range gates with the lowest centered at 1.75 km above ground level (AGL) and with a time resolution that varied during the five years of observations, but which was never longer than a few minutes. Here we present data from only the vertical and N and E beams at the 2.5-, 4.0-, 5.5-, and 7.0-km range gates. Data in the lowest range gate at 1.75 km were not usable due to the recovery time of the transmit/receive switch and data from range gates higher than the 7.0-km gate were intermittent due to the decreased signal-to-noise ratio.

It was not possible to develop an automatic process to apply wavelet analysis to the radar wind profiles, principally because the quality of radar time series is often vitiated by spurious signals and data gaps. The spurious signals are due to airplanes, lightning, meteors, and, rarely, heavy precipitation, each of which results in spurious spikes in the time series of wind in a given range gate. Data gaps occurred when the recording media were changed and when there were power outages, which did not affect the battery-driven barograph systems. Also, it is well known that wind fields are intrinsically more noisy than the ground pressure because, while the pressure is proportional to the integrated mass of the entire column of air above the barograph, the wind field is affected by local fluctuations that may not be present at all heights.

For illustration, we selected a period in 1993. The raw and extracted pressure traces at FLA from day 221.0 to 222.5 are shown in the third row of Fig. 6 and the highpass-filtered pressure trace $f_1(t)$ and corresponding wavelet transform magnitude $|W(b, a)|$ from day 220.0 to 224.0 are shown in the bottom row of Fig. 15. The wavelet analysis process described in Section 3 extracted two overlapping events. The propagation velocity could be determined for the event centered at about day 222.0, which was thus a CE, but not for the event centered at about day 222.5, which was thus an IE.

The time series of the radial wind from the north radar beam at 2.5, 4.0, 5.5, and 7.0 km and the corresponding wavelet transforms are shown in the top four rows of Fig. 15. Both events are evident at all altitudes between 2.5 and 7.0 km, particularly in the wavelet transform plots. However, the signatures of the events vary a great deal as a function of height. Since the radar wind data have not been highpass filtered, there is also a significant

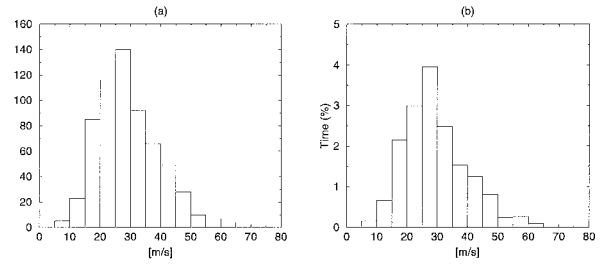

FIG. 10. Histograms of speed for CEs. The vertical axis indicates in (a) the number of events and in (b) their frequency of occurrence expressed as a percentage of the total analyzed time.

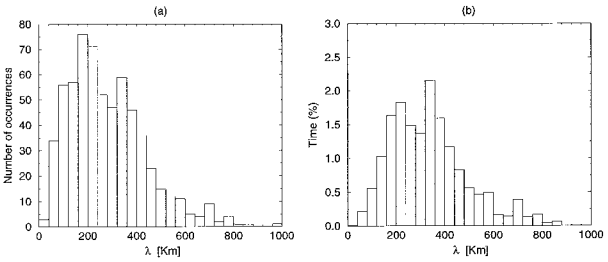

FIG. 12. Same as in Fig. 10 but for horizontal wavelengths λ of CEs.

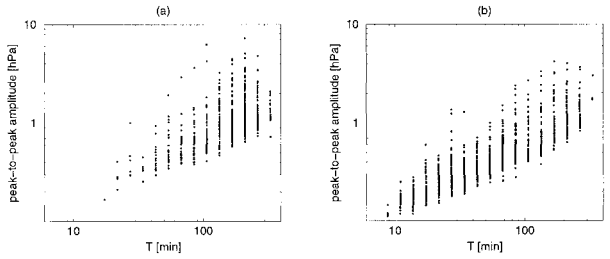

FIG. 13. Peak-to-peak amplitude versus dominant period T_m for (a) CEs and (b) IEs.

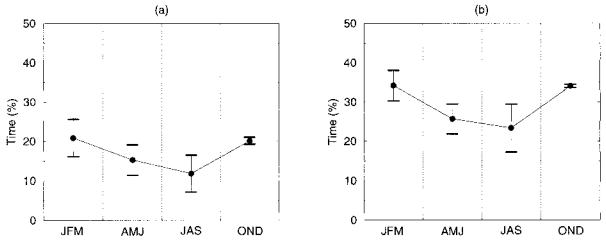

FIG. 14. Percentage time of occurrence for (a) CEs and (b) all events in different quarters. The circles are the percentages of observation time containing events averaged over the different years, and the bar intervals indicate the standard deviations.

long-period contribution in the wavelet transform, especially at 5.5 and 7.0 km in Fig. 15, mainly due to the ≈12 h separation between the two events. This example shows that the design of an automatic data processing technique for wind time series could be a rather challenging task. In fact, even if a strong ''qualitative'' correlation was detected between different heights, it seems to us quite complicated to define quantitative criteria and good statistical tests to be applied with success in an automatic fashion. This would have to be done case by case (see next paragraph). The variability with height would make the results of an automatic analysis difficult to interpret even with prior knowledge of the time–frequency signatures of the events in the pressure field.

Nevertheless, the radar data can be analyzed qualitatively to infer the vertical extent of an event that has been identified by wavelet analysis of the surface pressure data. We have done such an analysis around the times of the 64 pressure events with peak-to-peak amplitudes larger than 2 hPa in the extracted waveforms. There existed simultaneous radar data for the oblique beams in 21 cases and for the vertical beam in 20 cases. From inspection of the time series of wind at each height for each event we determined whether or not there was a corresponding event in the wind data. The statistics in Table 2 show that 60%–70% of the pressure events had wind signatures at 5.5 km and more than half of them had signatures at 7.0 km, the highest range gate with consistently good radar data. It seems likely that many of these events extended throughout the entire troposphere.

Studies of individual events will allow more quantitative conclusions on the interpretation of the radar data. Even in the presence of convection, by using additional meteorological data, including weather radar data, one might be able to separate the wind components due to periodic disturbances from the motions due to convection itself. We must, however, recognize that with the automatic process presented in this paper, the radar data can only provide qualitative information.

5. Relation to meteorological features

This section presents an attempt to discover the causes of the events by comparing the propagation speeds and directions of CEs and nearly simultaneous meteorological features. Three kinds of features have been considered: precipitation; surface boundaries, defined in section 5b; and dynamical instabilities at altitudes above 1 km inferred from radiosonde balloon wind and temperature profiles from the Peoria, Illinois, radiosonde station, about 130 km NW of FAO.

The present comparisons must be considered only semiquantitative and preliminary. We have analyzed pressure data automatically using a robust and relatively simple algorithm. We do not believe that similar algorithms can be applied to the analysis of other meteorological data from meteorological radars, wind profilers, surface stations, rawindsondes, etc. As a result, the establishment of the relation of gravity waves to meteorological features would require a case study approach.

a. Precipitation

The presence of precipitation at FAO was estimated from the National Centers for Environmental Prediction (NCEP) 3-hourly surface charts, the NCEP hourly radar summary charts, and the rain gauge at FAO. Although only 16% of all events were associated with precipitation, 73% of the CEs with amplitudes larger than 2 hPa were associated with precipitation on the NCEP charts and/or on the rain gauge data at FLA. Thus, the large events and precipitation appear to be associated.

b. Surface boundaries

We recorded the time of passage at FAO and the speed and direction of every surface meteorological feature displayed on the NCEP charts from 1991 through 1995. These features, here called surface boundaries, include cold fronts, warm fronts, stationary fronts, occluded fronts, squall lines, outflow boundaries, and troughs. Although the following statistics refer to all of these features without distinction, almost 80% of them were frontal passages. The time of passage and propagation speed and direction of a feature were determined by linear interpolation between successive surface charts. The direction was assumed to be perpendicular to the

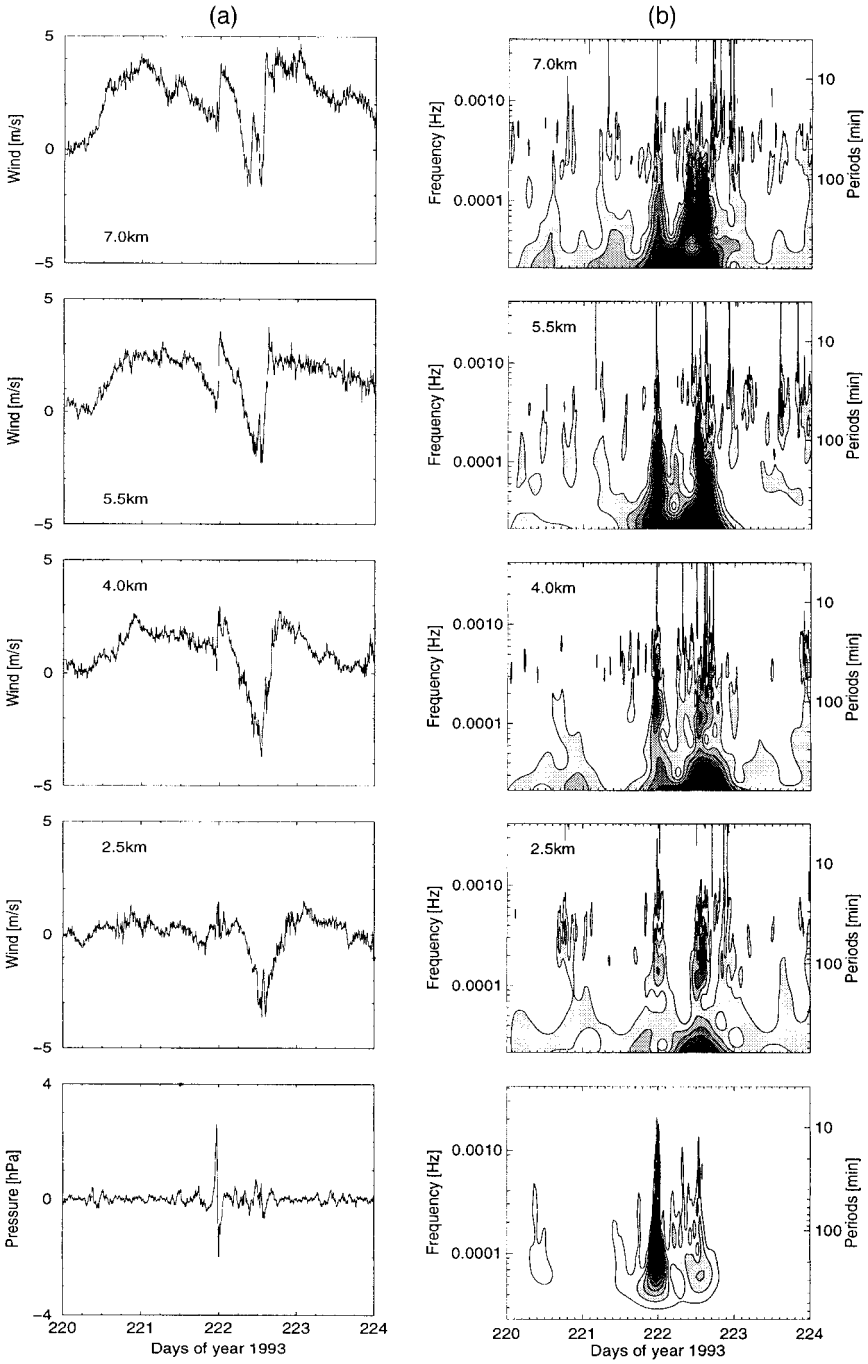

FIG. 15. (a) Raw radial wind traces from the VHF radar north-looking beam (top four rows) and highpass-filtered ground pressure $f_1(t)$ at FLA (last row). (b) Corresponding wavelet transform magnitudes $|W(b, a)|$; the grayscale is proportional to the wavelet magnitude.

boundary displayed on the charts. A more detailed analysis would have recognized that the air motion within a feature is generally oblique to the boundary, with the obliquity varying with altitude above the ground. Thus, the velocity of a wave generated by a feature may also be oblique. This could be studied by using the 915-MHz boundary layer radar that operated at FAO during part of the observation period to measure the wind within the front as a function of altitude.

On the 1301 days with usable barometer data, the wavelet algorithm extracted 626 CEs. A total of 169 of these events occurred within 6 h of a boundary passage on 147 separate days, with 41% preceding, 41% simultaneous with, and 18% following the boundary. Ta-

TABLE 2. Percentage of CEs with amplitude larger than 2 hPa having a signature in the wind fields at the different heights for the three Flatland VHF Doppler radar beams.

Height (km)	Oblique east beam (%)	Oblique north beam (%)	Vertical beam (%)
7.0	41	53	67
5.5	63	75	63
4.0	74	80	74
2.5	58	68	82

TABLE 3. Classification of the days in the investigated period (1991–95) based on the passage of surface boundaries through the network. Here $|\Delta t|$ denotes the time difference between the surface boundary and the pressure event.

415 days with at least one surface boundary	
147 days with CE within $\|\Delta t\| < 6$ h	35%
179 days with CE with $\|\Delta t\| > 6$ h and/or IE events	43%
89 days with no pressure events	22%
475 days with at least one CE	
147 days with surface boundary within $\|\Delta t\| < 6$ h	31%
328 days with no surface boundary within $\|\Delta t\| < 6$ h	69%

ble 3 summarizes the statistics on the number of days having extracted CEs or IEs and the number of days with at least one boundary passage.

We did not find any significant correlation between the speeds and directions of individual CEs and corresponding boundary passages. The mean speeds of the boundary passages were only 13.6 m s^{-1} compared with 27.5 m s^{-1} for the pressure events. On the other hand, the statistical distributions of the directions are similar.

c. Dynamical instabilities

It is well known that gravity waves can be generated by shear instability. In particular, jet streams have been shown to be a source of gravity waves (Mastrantonio et al. 1976) and to be a guiding mechanism for mesoscale waves as discussed by Lindzen and Tung (1976), Stobie et al. (1983), Uccellini and Koch (1987), and Ferretti et al. (1988). Indeed, the speed histograms, Fig. 10, show a peak in the 25–30 m s^{-1} range, well within typical values of the jet streams, while the histograms of direction, Fig. 9, indicate that the overwhelming majority of the disturbances move in the eastward direction $\pm 90°$, that is, in the general direction of the jet streams and jet streaks.

To establish wind shear as a source of these disturbances, one would have to carry out a detailed stability analysis (Mastrantonio et al. 1976) over a broad region, which is beyond the scope of the present study. However, we did do an approximate stability analysis at a single station. Since we could not do the analysis using the temporally high resolution radar wind profiles at FAO due to the lack of concurrent temperature profiles, we instead analyzed radiosonde profiles of wind and temperature from the nearest National Weather Service station at Peoria, Illinois, about 130 km northwest of FAO, following the methodology described by Keliher (1975). While we did not find a one-to-one correspondence between the predicted and observed directions and speeds of individual events, we observed that the histograms of the directions and speeds of the unstable regions above 5 km were quite similar to the observed histograms in Fig. 9 and 10. The lack of a detailed correlation is perhaps not surprising since Peoria is far from the region of maximum jet stream and jet streak activity.

Uccellini and Koch (1987) also discuss geostrophic adjustment as a source for these disturbances. They point out that mesoscale waves tend to occur in a common synoptic setting below highly ageostrophic regions associated with the upper-tropospheric jet streak system and that they can be an intrinsic part and owe their origin to the geostrophic adjustment process.

6. Conclusions

We have presented a climatology of large-amplitude disturbances using data from a network of sensitive digital barometers located around the Flatland Atmospheric Observatory near Champaign–Urbana, Illinois. The data cover 15 quarters from 1991 to 1995. The characteristic temporal and spatial scales of the processed data are limited by two factors. First, the size of the network, with distances between stations ranging from 5 to 50 km, does not allow a full analysis of events with periods smaller than ≈30 min. Second, a preprocessing highpass filter was applied to the data to remove fluctuations with periods longer than 6 h. Consequently, the characteristic horizontal scales range from a few tens to a few hundreds of kilometers.

Typical waveforms are localized in time, as shown in Fig. 6. A powerful and selective filtering technique based on the wavelet transform is utilized. This method provides objective localization of a disturbance and an accurate extraction of its waveform at each station through the selective inclusion of its time–frequency components. The application of a cross-correlation technique to the extracted waveforms is then used to determine the horizontal speed and direction of propagation for those events that are coherent through the network. This class of events, denoted CEs (coherent events), is characterized by mean cross-correlation values larger than 0.75. Another class of events, denoted IEs (incoherent events), includes disturbances with worse correlation or large variability in the estimates for speed and direction, and it also includes those coherent waves whose wavelength is too short relative to the size of the network. For these last disturbances an estimate of the propagation velocity was not determined due to the complication of aliasing.

Only disturbances with amplitudes larger than a threshold function are considered. This threshold, a

function of the dominant period, was obtained by averaging over the entire dataset. Typical amplitude values for the detected events, both CEs and IEs, ranged from about 0.3 hPa at 30 min to about 1 hPa at 4 h.

There are some limitations in the analysis method utilized. First, it is not appropriate for the study of nearly monochromatic waves lasting for several periods. In that case standard FFT techniques could be used. Second, it cannot track disturbances whose speed and direction are strongly varying functions of time and/or space. In cases such as arc-shaped disturbances, time-to-space conversion objective analysis can be used (Koch and O'Handley 1997). Third, it identifies as separate those events that might have been generated by a single phenomenon. In the case of a thunderstorm, for example, it cannot recognize that its various dynamical stages have different signatures in the pressure field, even though they are related to a common origin. Fourth, it cannot separate waves with the same period content that occur at the same time. Only events with distinct and separate signatures in the time–frequency plane can be processed with accuracy. On the other hand, the presented method is not limited to pressure time series analysis, but can be used to analyze geophysical data of various nature from any network of at least three instruments. The network should be sized according to the range of wavelengths, periods, and propagation speeds of the disturbances to be investigated. Of course, the wavelet analysis and filtering tools must be tuned to the data being processed. For a more detailed discussion we refer to GE98 and to the references therein.

The statistics presented in this paper show that the frequency of occurrence of events has a strong seasonal dependence, with a maximum in fall and winter and a minimum in summer. Of the total analyzed time, CEs occurred 20%–21% in fall and winter and 12% in summer, while all events occurred 34% in both fall and winter and 23% in summer. The percentages above are smaller than those given by Einaudi et al. (1989), who used a network of eight microbarographs deployed within a 500-m radius near Erie, Colorado. One should note, however, that (i) Erie is about 25 km east of the foothills of the Colorado Rocky Mountains where the level of mesoscale activity is greater than at locations away from mountains (Canavero and Einaudi 1987); (ii) the size of the Erie network and the mechanical response of the microbarographs filtered out disturbances with periods longer than about 20 min, so that there was essentially no overlapping of characteristic temporal scales with the present study; and (iii) the present analysis imposes rather stringent conditions on the identification of the truly coherent disturbances.

The histograms of periods show a distribution that covers the whole range of investigated timescales. Both the number of CEs and their frequency of occurrence increase with increasing period. The horizontal wavelength histograms show that almost all wavelengths were in the range between 40 and 600 km. The histograms show a decay of the number of occurrences for periods longer than about 4 h and horizontal wavelengths longer than about 350 km due to the preprocessing highpass filter applied to the data.

The speed histograms show a peak in the 25–30 m s^{-1} range, well within typical values of the jet stream, while the histograms of direction indicate that the overwhelming majority of the disturbances moves in the eastward direction $\pm 90°$, that is, in the general direction of the jet streams and jet streaks.

The identification of the source of a disturbance is often difficult even in the context of a detailed case study, since the source may not be in the neighborhood of the observation site and since the weather in the area of generation is often quite complex. Furthermore, tracking a disturbance far away from the observation site may require data recorded at standard surface stations. These unfortunately often have poor temporal resolution. We have nevertheless attempted to relate the observed events to meteorological features in the neighborhood of the observation network. These are some of the results.

1) The CEs were correlated only weakly if at all with the surface meteorological features that were investigated. However, 27% of the CEs occurred within 6 h of a boundary passage. Most of the CEs preceded the associated boundary passages or crossed the network at the same time. There was no significant correlation between the directions of propagation, but coherent pressure events generally moved faster than the associated weather events. This does not necessarily imply that the motion of a boundary passage is itself the source of the disturbances; rather, they may both be simply a manifestation of a baroclinic environment that is conducive to the generation and propagation of the waves as discussed earlier.
2) Several disturbances occurred without any charted boundary passage or precipitation activities.
3) There were some intervals lasting several days during which no events were detected. During these intervals there were also no significant meteorological features identified in the surface charts.
4) Precipitation was present with 73% of the large-amplitude CEs.
5) About 40% of the large disturbances presented features typical of solitary waves. We included in this category event types I–IV reported in Fig. 6. They occurred with the general characteristics discussed in 1–4 above. Their largest number of occurrences had periods just below 4 h with a broad distribution in horizontal scales ranging from 30 to 400 km. While none of the cases identified in this study reached the amplitude of that presented by Schneider (1990), this analysis confirms that this particular type of disturbance appears to be an important component of the dynamical behavior of the atmosphere at the mesoscale.

Although an automatic analysis of the wind profiles obtained from a 50-MHz Doppler radar at the Flatland Atmospheric Observatory was not possible for the reasons mentioned in section 4, we performed a qualitative analysis of the depth of the disturbances with amplitude larger than 2 hPa. The results show that in most cases the events also have a strong signature in the wind fields and that this signature is visible at least up to 7 km AGL, which was the height limit dictated by the radar sensitivity. Thus, these disturbances involve the entire troposphere.

A detailed analysis of a few cases involving large-amplitude events is in progress to determine more accurately their source mechanisms and the synoptic environment conducive to their propagation.

Acknowledgments. We wish to thank L. W. Uccellini of the Office of Meteorology of NOAA and J. G. Stobie of SAIC at NASA/GSFC for useful discussions and comments. We also acknowledge constructive suggestions made by three anonymous reviewers. The barometer network was supported in part by the Aeronomy Laboratory of NOAA and in part by NASA Headquarters. S. E. Hollinger of the Illinois State Water Survey assisted in locating and installing the barometer sites, which were provided gratis by citizens and organizations, and S. W. Henson of the University of Illinois, Urbana–Champaign, provided operational support. Research at the Aeronomy Laboratory was supported in part by the Division of the Atmospheric Sciences of the National Science Foundation by Grants ATM-9319085 and 9419638.

REFERENCES

Allen, S. J., and R. A. Vincent, 1995: Gravity wave activity in the lower atmosphere: Seasonal and latitudinal variations. *J. Geophys. Res.,* **100,** 1327–1350.

Bacmeister, J. T., 1993: Mountain-wave drag in the stratosphere and mesosphere inferred from observed winds and a simple mountain-wave parameterization scheme. *J. Atmos. Sci.,* **50,** 377–399.

Balachandran, N. K., 1980: Gravity waves from thunderstorms. *Mon. Wea. Rev.,* **108,** 804–816.

Barnes, S. L., F. Caracena, and A. Marroquin, 1996: Extracting synoptic-scale diagnostic information from mesoscale models: The Eta model, gravity waves, and quasigeostrophic disgnostics. *Bull. Amer. Meteor. Soc.,* **77,** 519–528.

Bedard, A. J., Jr., F. Canavero, and F. Einaudi, 1986: Atmospheric gravity waves and aircraft turbulence encounters. *J. Atmos. Sci.,* **43,** 2838–2844.

Bosart, L. F., and J. P. Cussen, 1973: Gravity wave phenomena accompanying east coast cyclogenesis. *Mon. Wea. Rev.,* **101,** 446–454.

Bull, G., R. Dubois, J. Neisser, and J.-G. Stangenberg, 1981: Untersuchungen über Schwerewellen in Gebirgsnähe. *Z. Meteor.,* **31,** 267–279.

Canavero, F., and F. Einaudi, 1987: Time and space variability of spectral estimates of atmospheric pressure. *J. Atmos. Sci.,* **44,** 1589–1604.

Christie, D. R., 1989: Long nonlinear waves in the lower atmosphere. *J. Atmos. Sci.,* **46,** 1462–1491.

——, 1992: The morning glory of the Gulf of Carpentaria: A paradigm for non-linear waves in the lower atmosphere. *Aust. Meteor. Mag.,* **41,** 21–60.

Chui, C. K., 1992: *An Introduction to Wavelets. Wavelet analysis and Its Applications.* Vol. 1. Academic Press, 264 pp.

Clark, T. L., and T. Thomas, 1986: Convectively forced internal gravity waves: Results from two-dimensional numerical experiments. *Quart. J. Roy. Meteor. Soc.,* **112,** 899–925.

Daubechies, I., 1992: *Ten Lectures on Wavelets.* CBMS–NSF Series in Applied Mathematics, Vol. 61, SIAM 357 pp.

Einaudi, F., 1995: Gravity waves in the troposphere. *Diagnostic Tools in Atmospheric Physics,* G. Fiocco and G. Visconti, Eds., IOS Press, 307–340.

——, and J. J. Finnigan, 1981: The interaction between an internal gravity wave and the planetary boundary layer. Part I: The linear analysis. *Quart. J. Roy. Meteor. Soc.,* **107,** 793–806.

——, A. J. Bedard, and J. J. Finnigan, 1989: A climatology of gravity waves and other coherent disturbances at the Boulder Atmospheric Observatory during March–April 1984. *J. Atmos. Sci.,* **46,** 303–329.

Ferretti, R., F. Einaudi, and L. W. Uccellini, 1988: Wave disturbances associated with the Red River Valley severe weather outbreak of 10–11 April 1979. *Meteor. Atmos. Phys.,* **39,** 132–168.

Fritts, D. C., and W. Lu, 1993: Spectral estimates of gravity wave energy and momentum fluxes. Part II: Parameterization of wave forcing and variability. *J. Atmos. Sci.,* **50,** 3695–3713.

Fulton, R., D. S. Zrnic, and R. J. Doviak, 1990: Initiation of a solitary wave family in the demise of a nocturnal thunderstorm density current. *J. Atmos. Sci.,* **47,** 319–337.

Gossard, E. E., 1960: Spectra of atmospheric scalars. *J. Geophys. Res.,* **65,** 3339–3351.

Grivet-Talocia, S., and F. Einaudi, 1998: Wavelet analysis of a microbarograph network. *IEEE Trans. Geosci. Remote Sens.,* **36,** 418–433.

Grossmann, A., R. Kronland-Martinet, and J. Morlet, 1989: Reading and understanding continuous wavelet transform. *Wavelets, Time-Frequency Methods and Phase Space,* J. M. Combes, A. Grossmann, and P. Tchamitchian, Eds., Springer-Verlag, 1–20.

Hauf, T., and T. L. Clark, 1989: Three-dimensional numerical experiments on convectively forced internal gravity waves. *Quart. J. Roy. Meteor. Soc.,* **115,** 309–333.

——, U. Finke, J. Neisser, G. Bull, and J.-G. Stagenberg, 1996: A ground-based network for atmospheric pressure fluctuations. *J. Atmos. Oceanic Technol.,* **13,** 1001–1023.

Herron, T. J., and I. Tolstoy, 1969: Tracking jet stream winds from ground level pressure signals. *J. Atmos. Sci.,* **26,** 266–269.

Hines, C. O., 1997a: Doppler-spread parameterization of gravity-wave momentum deposition in the middle atmosphere. Part 1: Basic formulation. *J. Atmos. Sol. Terr. Phys.,* **59,** 371–386.

——, 1997b: Doppler-spread parameterization of gravity-wave momentum deposition in the middle atmosphere. Part 2: Broad and quasi monochromatic spectra, and implementation. *J. Atmos. Sol. Terr. Phys.,* **59,** 387–400.

Hirota, I., 1984: Climatology of gravity waves in the middle atmosphere. *J. Atmos. Terr. Phys.,* **46,** 767–773.

——, and T. Niki, 1985: A statistical study of inertia-gravity waves in the middle atmosphere. *J. Meteor. Soc. Japan,* **63,** 1055–1065.

Hooke, W. H., and K. R. Hardy, 1975: Further study of the atmospheric gravity waves over the eastern seaboard on 18 March 1969. *J. Appl. Meteor.,* **14,** 31–38.

Keliher, T. E., 1975: The occurrence of microbarograph-detected gravity waves compared with the existence of dynamically unstable wind shear layers. *J. Geophys. Res.,* **80,** 2967–2976.

Kitamura, Y., and I. Hirota, 1989: Small-scale disturbances in the lower stratosphere revealed by daily rawinsonde observations. *J. Meteor. Soc. Japan,* **67,** 817–830.

Koch, S. E., and C. O'Handley, 1997: Operational forecasting and detection of mesoscale gravity waves. *Wea. Forecasting,* **12,** 253–281.

Koppel, L. L., L. F. Bosart, and D. Keyser, 1999: A 25-yr climatology

of large-amplitude hourly surface pressure changes over the conterminous United States. *Mon. Wea. Rev.,* in press.

Lau, K.-M., and H. Weng, 1995: Climate signal detection using wavelet transform: How to make a time series sing. *Bull. Amer. Meteor. Soc.,* **76,** 2391–2402.

Lindzen, R. S., and K. K. Tung, 1976: Banded convective activity and gravity waves. *Mon. Wea. Rev.,* **104,** 1602–1617.

Mastrantonio, G., F. Einaudi, D. Fua, and D. P. Lalas, 1976: Generation of gravity waves by jet streams in the atmosphere. *J. Atmos. Sci.,* **33,** 1730–1738.

Mayr, H. G., J. G. Mengel, C. O. Hines, K. L. Chan, N. F. Arnold, C. A. Reddy, and H. S. Porter, 1997a: The gravity wave Doppler spread theory applied in a numerical spectral model of the middle atmosphere. Part I: Model and global scale seasonal variations. *J. Geophys. Res.,* **102** (D22), 26 077–26 091.

——, ——, ——, ——, ——, ——, and ——, 1997b: The gravity wave Doppler spread theory applied in a numerical spectral model of the middle atmosphere. Part II: Equatorial oscillations. *J. Geophys. Res.,* **102** (D22), 26 093–26 105.

McFarlane, N. A., 1987: The effect of orographically excited gravity wave drag on the general circulation of the lower stratosphere and troposphere. *J. Atmos. Sci.,* **44,** 1775–1800.

Mengel, J. G., H. G. Mayr, K. L. Chan, C. O. Hines, C. A. Reddy, N. F. Arnold, and H. S. Porter, 1995: Equatorial oscillations in the middle atmosphere generated by small scale gravity waves. *Geophys. Res. Lett.,* **22,** 3027–3030.

Meyer, Y., 1992: *Wavelets and Operators. Cambridge Studies in Advanced Mathematics.* Vol. 37, Cambridge University Press, 223 pp.

Murayama, Y., T. Tsuda, and S. Fukao, 1994: Seasonal variation of gravity wave activity in the lower atmosphere observed with the MU radar. *J. Geophys. Res.,* **99,** 23 057–23 069.

Nastrom, G. D., T. E. Van Zandt, and J. M. Warnock, 1997: Vertical wavenumber spectra of wind and temperature from high-resolution balloon soundings over Illinois. *J. Geophys. Res.,* **102,** 6685–6701.

Pokrandt, P. J., G. J. Tripoli, and D. D. Houghton, 1996: Process leading to the formation of mesoscale gravity waves in the Midwest cyclone of 15 December 1987. *Mon. Wea. Rev.,* **124,** 2726–2752.

Powers, J. G., 1997: Numerical model simulation of mesoscale gravity-wave event: Sensitivity test and spectral analyses. *Mon. Wea. Rev.,* **125,** 1838–1869.

Ralph, F. M., M. Crochet, and S. V. Venkateswaran, 1993: Observations of a mesoscale ducted gravity wave. *J. Atmos. Sci.,* **50,** 3277–3291.

Sato, K., 1994: A statistical study of the structure, saturation and sources of inertio-gravity waves in the lower stratosphere observed with the MU radar. *J. Atmos. Terr. Phys.,* **56,** 755–774.

Schmidt, J. M., and W. R. Cotton, 1990: Interaction between upper and lower tropospheric gravity waves on squall line structure and maintenance. *J. Atmos. Sci.,* **47,** 1205–1222.

Schneider, R. S., 1990: Large-amplitude mesoscale wave disturbances within the intense Midwest extratropical cyclone of 15 December 1987. *Wea. Forecasting,* **5,** 533–558.

Smith, R. K., 1988: Traveling waves and bores in the lower atmosphere: The ''morning glory'' and related phenomena. *Earth Sci. Rev.,* **25,** 267–290.

Stobie, J. G., F. Einaudi, and L. W. Uccellini, 1983: A case study of gravity waves–convective storms interactions: 9 May 1979. *J. Atmos. Sci.,* **40,** 2804–2830.

Uccellini, L. W., 1975: A case study of apparent gravity wave initiation of severe convective storms. *Mon. Wea. Rev.,* **103,** 497–513.

——, and S. E. Koch, 1987: The synoptic setting and possible energy sources for mesoscale wave disturbances. *Mon. Wea. Rev.,* **115,** 721–729.

Warner, C. D., and M. E. McIntyre, 1996: On the propagation and dissipation of gravity waves through a realistic middle atmosphere. *J. Atmos. Sci.,* **53,** 3213–3234.

Wilson, R., M. L. Chanin, and A. Hauchecorne, 1991: Gravity waves in the middle atmosphere observed by Rayleigh lidar. 2. Climatology. *J. Geophys. Res.,* **96,** 5169–5183.